# Strain and Optoelectronic Tuning in Mixed-Halide Perovskites with Ion Irradiation

Subodh SK Gautam, Minjin Kim, Bernard Geffroy, Milo Boirot, Vincent Jacques, Olivier Plantevin

ADVANCED OPTICAL MATERIALS
www.advopticalmat.de

# Strain and Optoelectronic Tuning in Mixed-Halide Perovskites with Ion Irradiation

*Subodh K. Gautam,* Minjin Kim, Bernard Geffroy, Milo Boirot, Vincent L. R. Jacques, and Olivier Plantevin**

**Defects usually behave as imperfections in materials that significantly degrade their performance. However, the unusual optoelectronic performance in metal halide perovskites in the presence of defects opens the way for strain and optoelectronic properties tailoring with ion irradiation. Defects and strain engineering is performed in triple-cation mixed halide perovskites using proton irradiation at 1 MeV and different fluences. At intermediate fluence, the initial polycrystalline film compressive strain (−0.15%) can be released, improving exciton lifetimes from about 500 ns to ≈1 µs. In contrast, high irradiation fluence is shown to restore compressive strain leading to sample degradation, with lower lifetime values (≈200 ns). Also, the phase segregation occurring under light illumination between bromine-rich and iodine-rich regions is shown to be defects-mediated as the segregation rate increases by a factor of four for high proton irradiation fluence. The irradiation defects are revealed with low-temperature photoluminescence (PL) through bound exciton radiative recombination mechanisms. The PL temperature dependence gives some insight into electron–phonon coupling mechanism and their modification with ion irradiation.**

## 1. Introduction

Hybrid organic–inorganic perovskites have become one of the most promising low-cost alternatives to traditional semiconductors in photovoltaics and light-emitting devices. It combines both attractive features of organic and inorganic materials within a single composite, for instance, with more robust excitonic properties and brighter luminescence than inorganic semiconductors together with high ambipolar mobilities, about few tens $cm^2\ V^{-1}\ s^{-1}$ for mixed-halide perovskites,[1,2] several orders of magnitude larger than in organic semiconductors. The most frequently used material in high-performing perovskite solar cells is methylammonium lead tri-iodide ($CH_3NH_3PbI_3$, referred to as $MAPbI_3$) which has a tetragonal structure at room temperature. This material undergoes two structural phase transitions as a function of increasing temperature: from orthorhombic to tetragonal at 160 K and from tetragonal to cubic at about 310 K.[3] The material is generally synthesized at temperatures about 350 K in the cubic phase, and must reorganize when crossing the structural phase transition to stabilize in the tetragonal phase at room temperature. This phase is thus composed of several domains, given the three variants being equally probable, that might introduce many atomic and extended defects. This presence of many defects within the perovskite materials is thus of primary interest to get a complete understanding of their electronic properties.[4] Theoretical calculations revealed that the electronic properties of metal halide perovskites (MHP) are tolerant to defects because the intrinsic point defects and grain boundaries do not generate in-gap states.[5] Also, it was predicted that the electronic conductivity of perovskite could be tuned between p-type and n-type by controlling growth conditions. This self-doping effect in $CH_3NH_3PbI_3$ was then reported and found to be either n- or p-type by changing the ratio of methylammonium halide (MAI) and lead iodide ($PbI_2$), which are the two precursors for perovskite formation.[6] The n-type doping was associated with iodine vacancies, having the lowest formation energy, while the p-type behavior was associated with Pb vacancies. Regarding the optoelectronic properties, it was recently shown that the defects behave in an unusual way in MHP, acting primarily as trapping and release centers without non-radiative recombination, resulting in efficient photoconversion and charge transport properties.[7] However, defect tolerance and defect passivation has become a challenge to improve efficiencies in the frame of photovoltaic devices[8] and was shown to be a foreground issue to understand hybrid perovskite materials[9] in particular regarding their impact on carrier recombination, charge transport and limitations in power

S. K. Gautam, M. Boirot, V. L. R. Jacques, O. Plantevin
Laboratoire de Physique des Solides, CNRS UMR8502
Université Paris-Saclay
91405 Orsay, France
E-mail: subodh-kumar.gautam@uvsq.fr;
olivier.plantevin@universite-paris-saclay.fr
M. Kim, B. Geffroy
Institut Polytechnique de Paris
route de Saclay, 91128 Palaiseau, France

The ORCID identification number(s) for the author(s) of this article can be found under https://doi.org/10.1002/adom.202300577



**DOI: 10.1002/adom.202300577**

conversion efficiencies in solar cell devices.[10,11] Defects are usually regarded as imperfections in semiconductor materials that could significantly degrade their performance. However, controlling their formation may be beneficial to generate novel properties and tailor their properties for device applications. Furthermore, perovskite films also exhibit some degree of lattice strain, affecting their structural stability and optoelectronic properties, though it is still under debate how the strain, affects the carrier recombination process and other optoelectronic properties.[12–14] Here, we carry out defect engineering applied to mixed-halide hybrid organic–inorganic perovskites using ion irradiation to introduce point defects in a controlled manner. We show that irradiation defects influence thin film strain, optoelectronic properties, and phase segregation dynamics.

To date, various combinations and ratios of monovalent organic and inorganic cations (formamidinium FA, methylammonium MA, and cesium Cs) and halides (I and Br) have been optimized for the band gap tuning as a means of improving the efficiency and stability of perovskite solar cells.[15–18] Therefore, multiple-cation mixed-halide (Cs, FA, MA)Pb(I, Br)$_3$ perovskite materials possess excellent properties with improved performance of photovoltaic devices. In the present study we will focus on such triple-cation-based hybrid perovskite films with a composition $(MA_{0.17}FA_{0.83})_{0.95}Cs_{0.05}Pb(I_{0.83}Br_{0.17})_3$.[15] We will quote TC-MHP for triple cation-mixed halide perovskites. Unfortunately, being optimized for better quality,[15] these mixed halide perovskites exhibit unwanted structural instabilities under continuous light irradiation. As initially reported, $MAPb(I_{1-x}Br_x)_3$ undergoes reversible halide phase segregation under light illumination into separate I- and Br-rich domains within the parent phase.[19] In recent years, it was reported that the light-induced phase segregation process in $MAPb(I_{1-x}Br_x)_3$ and $CsPb(I_{1-x}Br_x)_3$ perovskites is mainly related to the migration of iodine ions that segregate into iodine-rich clusters. Radiative recombinations are prone to occur in these iodine-rich clusters that show a lower energy band gap than the matrix.[20,21] Interestingly, as these clusters are enriched with iodine under illumination, their local iodine vacancy concentration is lowered. At the same time, the associated radiative recombination also shows an increased lifetime from about 0.8 to 4 µs.[21] Point defects affect the photo-induced halide mobility in MHP, which is one of today's challenges for improved stability in opto-electronic devices. In this work, 1 MeV proton irradiation has been used as a tool to tune the defect density in perovskite films in a controlled manner. The present study will help to understand better the light-induced phase separation phenomenon in TC-MHP films and the relationship between these mechanisms and native or irradiation-based point defects together with thin film strain.

## 2. Irradiation Effect on Mixed-Halide Perovskite

### 2.1. Ion Irradiation

We have introduced on purpose different defect concentrations into TC-MHP polycrystalline thin films, of composition $(MA_{0.17}FA_{0.83})_{0.95}Cs_{0.05}Pb(I_{0.83}Br_{0.17})_3$, with proton irradiation at 1 MeV and different fluences from $10^{13}$ cm$^{-2}$ to $5 \times 10^{15}$ cm$^{-2}$. Contrary to usual semiconductors, where irradiation defects quench the luminescence very efficiently, it was already observed that hybrid perovskite samples, both in single crystals and polycrystalline thin films, present high radiation hardness under Helium ion irradiation using low energy at 30 keV[22] or proton irradiation at 50 keV.[23] We estimated, for instance, that these compounds were about $10^5$ times more radiation-hard than crystalline silicon. At 30 keV and fluences from $10^{14}$ to $10^{15}$ cm$^{-2}$, only short lifetimes are impacted by the non-radiative decay paths introduced through ion irradiation. However, at higher fluence ($2 \times 10^{16}$ cm$^{-2}$), lifetime decreases more drastically. At higher energy, from 1 to 10 MeV, perovskite solar cells show good robustness up to $10^{11}$ protons cm$^{-2}$, depending on the nature of the hole transporting layer used for the device.[24] In the case of high energy proton (68 MeV), the radiation hardness of solar cells was evidenced up to fluences in the $10^{12}$ to $10^{13}$ cm$^{-2}$ range.[25] It was also shown that such high energy irradiation (at 68 MeV and $10^{13}$ cm$^{-2}$) could lead to solar cell device improvement through an increase in open circuit voltage, fill factor, and recombination lifetime of photogenerated charge carriers.[26] A 100% relative increase for PL decay time was reported after irradiation at 68 MeV and $2 \times 10^{12}$ cm$^{-2}$, for both devices and thin films, while the irradiation at 20 MeV for the same fluence did show almost no change.[27] More insights were given for (perovskite/CIGS) tandem solar cells that could be used for space applications with good radiation hardness up to $2 \times 10^{12}$ cm$^{-2}$.[28]

According to SRIM simulation results (see Figure S1, Supporting Information), the irradiation with 1 MeV protons leads to the formation of about 0.1 vacancies per incident ion along the ion beam trajectory within the thickness of our samples (about 400 nm), which is rather low as compared to 30 keV helium ion irradiation used in a previous study with about five vacancies per incident ion along the ion beam trajectory.[22,29] The projected range at 1 MeV is about 17 µm compared to 340 nm at 30 keV. At 30 keV, most irradiation particles stop in the material, thus creating a high number of end-of-range defects. The simulation evidence that the nuclear energy deposition (ballistic collisions) is about hundred times lower at 1 MeV compared to 30 keV within the thickness of the perovskite material for a given fluence. Interestingly we can also observe that the ratio between electronic energy loss and nuclear energy loss is about one thousand at 1 MeV as compared to two hundred at 30 keV, as discussed in the Section S2, Supporting Information.

### 2.2. Optoelectronic Properties

The effect of proton irradiation on the optical absorbance and PL emission of TC-MHP films was investigated, as represented in **Figure 1**a. The optical absorption spectra of pristine and irradiated films at significative irradiation fluences ($10^{14}$ cm$^{-2}$ and $5 \times 10^{15}$ cm$^{-2}$) are shown. All spectra show high absorbance of perovskite films for energies higher than 1.62 eV and exhibit a high absorbance coefficient of $\approx 10^4$ cm$^{-1}$. UV-vis spectra show relatively sharp near band edge absorption for a pristine film with direct band gap $E_g \approx 1.624$ eV, obtained from a classical Tauc analysis (see inset figure). The bandgap remains stable at this value after irradiation with moderate fluence up to $5 \times 10^{14}$ cm$^{-2}$. However, a significant blue shift is observed at higher fluence along with bending in the absorption band edge. An increase in the optical bandgap of ≈12 meV is observed with the

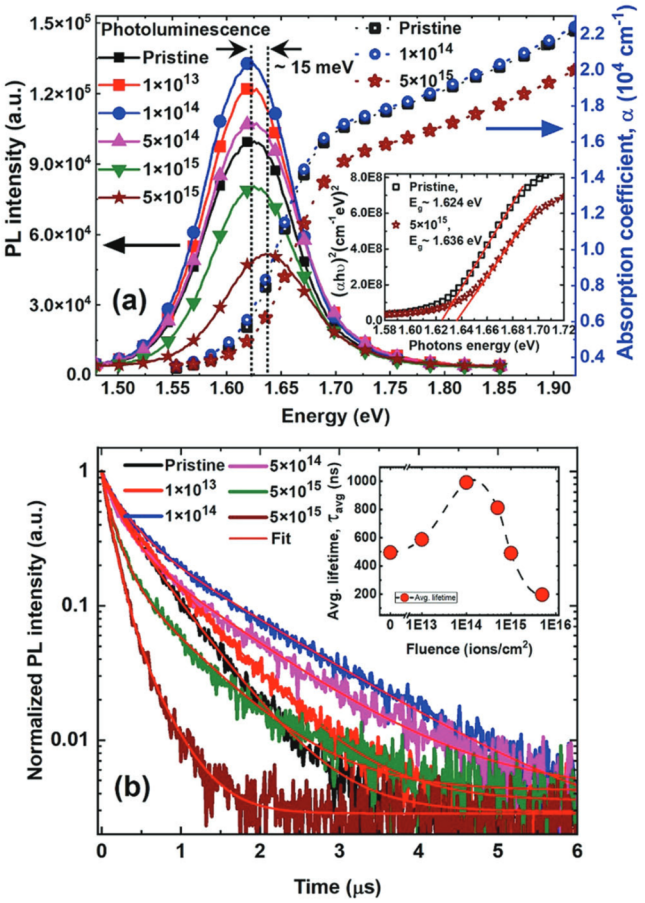


**Figure 1.** a) Photoluminescence spectra of triple-cation mixed-halide perovskite film as a function of proton irradiation fluence. Inset in (a) shows the UV–vis absorption data represented as $(\alpha h\nu)^2$ as a function of energy for the pristine and irradiated ($5 \times 10^{15}$ cm$^{-2}$) film. The dotted lines correspond to the Tauc plot analysis and the intercepts with the abscissa line is giving the bandgap values. b) Photoluminescence decay spectra of irradiated films at different fluences. Inset of (b): Average lifetime as a function of fluence extracted from the fits of PL decay curves.

highest fluence. The PL spectra of the TC-MHP films show a slight increase in PL intensity after irradiation in the range from $10^{13}$ cm$^{-2}$ to $5 \times 10^{14}$ cm$^{-2}$ with no noticeable shift or broadening. A slight increase of PL intensity after irradiation at high energy and low fluence was also reported in a previous work.[28] At higher fluences, from $10^{15}$ cm$^{-2}$ to $5 \times 10^{15}$ cm$^{-2}$, the PL intensity shows a relative decrease as compared to the pristine film. Consistent with the band gap modification observed with optical absorption, the PL emission peak also shows a significant shift (≈15 meV) to higher energy along with spectrum broadening. This broadening might be associated with several near-band-edge electronic defect levels associated with the high density of point defects and defect clusters created at high irradiation fluence. To understand the role of defect concentration on carrier dynamics, we have recorded the time-resolved PL decays of proton irradiated TC-MHP films at different fluences. Figure 1b shows normalized PL-decay spectra fitted with a double exponential decay fit, and the inset figure represents the calculated average PL lifetimes versus irradiation fluence. The lifetime is shown to increase from 478 ns to ≈1 µs after irradiation at moderate fluence from $10^{13}$ to $5\times 10^{14}$ cm$^{-2}$ and then decrease to 190 ns at the highest fluence of $5 \times 10^{15}$ cm$^{-2}$. We will further discuss this behavior in the next section in light of the structural changes. It is well known that trap-mediated recombination processes, previously known as Shockley–Read–Hall (SRH) recombination, dominate under low-carrier density and saturate after the free charge carrier density gets above ≈$10^{15}$ cm$^{-3}$ when band-to band bimolecular processes start dominating.[30,31] In this work, PL decay measurements were carried out using low-power (6 µW) excitation source with a repetition rate of 100 kHz. The initial carrier density is estimated ≈$4.45 \times 10^{14}$ cm$^{-3}$ with assuming that every incident photon generates a charge carrier. Pristine films follow a mono-exponential decay, which suggests that trap-mediated monomolecular recombination process (Shockley–Read–Hall) dominate the overall carrier dynamics and higher order recombination processes are negligible. The parameter values which return the best fit of PL decay curves are shown in Table S2, Supporting Information. The Shockley–Read–Hall rate constant ($R_{SRH}$) constant values are extracted from the long PL decay components of pristine and irradiated films. The $R_{SRH}$ is calculated and inversely follows the carrier lifetime at different fluences. For the pristine film the $R_{SRH}$ constant is ≈$-1.8 \times 10^6$ s$^{-1}$ which decreases to ≈$8.3 \times 10^5$ s$^{-1}$ for an irradiation fluence of $10^{14}$ cm$^{-2}$. The decrease in $R_{SRH}$ value confirms that the trap density reduces after irradiation with moderate fluence. However, it increases to ≈$3 \times 10^6$ s$^{-1}$ at the highest fluence of $5 \times 10^{15}$ cm$^{-2}$, above the initial value. The calculated $R_{SRH}$ for the pristine film agrees well with values reported for comparable perovskite compositions.[30] Furthermore, a fast-initial photoluminescence decay component evolves at higher irradiation fluences in the range $5 \times 10^{14}$ cm$^{-2}$–$5 \times 10^{15}$ cm$^{-2}$ when the irradiation defect density increases. This short decay reveals the rapid localization of free charge carriers in unoccupied high-density trap states, resulting in the reduction of the overall average carrier lifetime.

### 2.3. Thin Film Strain Modification with Ion Irradiation

The structural properties of pristine and irradiated films are studied by X-ray diffraction in Bragg–Brentano geometry. The diffractograms are represented in **Figure 2**. The TC-MHP films show polycrystalline nature due to their film growth at low temperatures based on the solution process. All diffractograms display the characteristic peaks of the cubic phase of TC-MHP, and agree with previous reports. An additional peak of $PbI_2$ is also observed, which is also typical in those systems. The structural changes are more visible at higher angles in XRD. Here, the strongest peak measured at relatively high angles is the 220 reflection, appearing at $2\theta$ ≈40.8° for the pristine film. Its evolution as a function of irradiation is shown in Figure 2b. For low-irradiation fluences, up to $10^{14}$ cm$^{-2}$, this reflection shifts to lower $2\theta$ angles, has a larger maximum peak intensity, and seems to get narrower. For higher irradiations, the inverse behavior is observed, and at $10^{15}$ cm$^{-2}$, the 220 peak is similar as in the pristine state. The change of width and maximum intensity can be explained by a change of crystallite size and lattice strain. In general, the presence of atomic interstitials and vacancies can lead to strain formation. In

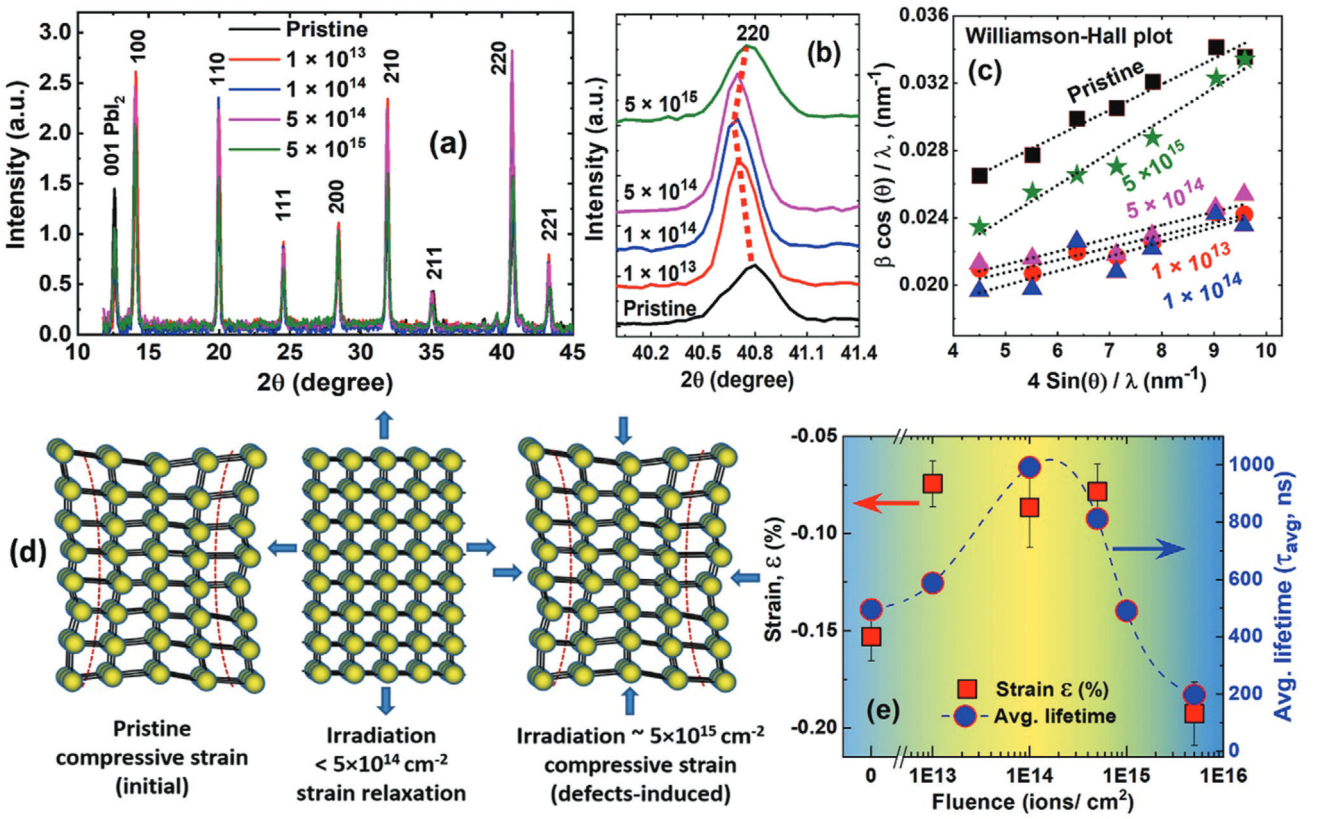


**Figure 2.** a) X-ray diffraction (XRD) spectra of triple-cation mixed-halide perovskite films at different irradiation fluences. b) (220) diffraction peak, the red dotted line illustrates the complex strain behavior as a function of irradiation fluences. c) Linear Williamson Hall plot of the XRD data for pristine and irradiated films at different fluences. d) Schematic for ion irradiation and strain modification on an MHP sample. e) Correlation between average carrier lifetime and compressive strain as a function of irradiation fluence (relative strain is estimated from WH analysis of the XRD measurements, and average lifetime is estimated from the TCSPC data).

particular, irradiation-induced point defects can modify the internal strain in the lattice. In this case, the changes of peak position and widths in diffraction are correlated and microstrain in the material can be determined by Bragg peak width analyses using the commonly employed Williamson-Hall (W-H) method.[14] This method is based upon the broadening analysis of the diffraction peaks and measures the relative deviations of peak positions from their average initial value to quantify the material's strain (compressive or tensile). The analysis is based upon a simplified method where both size-induced and strain-induced broadening are deconvoluted by considering the peak width as a function of $2\theta$. The width $\beta_{hkl}$ is taken as the sum of grain size broadening and strain-induced broadening as

$$\beta_{hkl} = \frac{K\lambda}{D\cos(\theta)} + 4\epsilon\tan(\theta) \quad (1)$$

where $K$ is a constant, $D$ is the average grain size, $\epsilon$ is the relative deformation, and $\beta$ is the Bragg peak width.

Thus

$$\frac{\beta_{hkl}\cos(\theta)}{\lambda} = \frac{K}{D} + \frac{4\epsilon\sin(\theta)}{\lambda} \quad (2)$$

The plot of $\frac{\beta_{hkl}\cos(\theta)}{\lambda}$ as a function of $\frac{4\sin(\theta)}{\lambda}$ for all peaks of the diffractogram allows to perform a linear fit and get the crystalline size from the $y$-intercept and the strain $\epsilon$ from the slope.

The W–H plot is represented in Figure 2c for all samples, and the slope from W-H plot analysis is determined for each irradiation fluence. The various parameters extracted from the W–H analysis and 220 diffraction peak are mentioned in the Table S1, Supporting Information. The pristine sample has a slope of $1.5 \times 10^{-3}$ which corresponds to a compressive strain of $\approx -0.15\%$. The native strain may arise due to the presence of defects during the growth process. At moderate irradiation fluence, W-H plot analysis reveals much lower slope value ($\approx 8.7 \times 10^{-4}$ ) which shows that the initial compressive strain relaxes after irradiation with fluences from $10^{13}$ to $5 \times 10^{14}$ cm$^{-2}$. The irradiation at moderate fluences could lead to local atomic mobility equivalent to defect annealing through electronic energy deposition and relax the intrinsic lattice strain. At a higher fluence of $10^{15}$ cm$^{-2}$, the W-H plot shows a higher slope value ($1.9 \times 10^{-3}$) close to the pristine film value, which confirms that the irradiated film returns into a compressive strain state ($\approx -0.19\%$) after the formation of a high density of defects. The whole scenario is represented schematically in Figure 2d, where lattice strain was evidenced under light illumination in TC-MHP.[32] To characterize the

irradiation effect on strain in perovskite lattice, we further analyze the response of the 220 diffraction peak position as a function of irradiation fluence, as represented in Figure 2b. The values of compressive/tensile strain are usually expressed as a ratio of the $d$ spacings and written as percentages. The strain $\epsilon(hkl)$ is determined here using the relative peak shift (relative change in lattice constant) of 220 Bragg peak (i.e., strain $\epsilon(hkl) = \frac{\delta a}{a}$). The reduction in compressive strain magnitude is observed after irradiation for fluences of $10^{13}$ and $10^{14}$ cm$^{-2}$ as the $2\theta$ angle of the 220 diffraction peak increases (lower $d$-spacing) after irradiation. This shift implies the lattice expansion related to strain relaxation of TC-MHP films, whereas as the irradiation fluence increases to $5 \times 10^{14}$ cm$^{-2}$ the peak position is constant and characteristic of a strain-free film (Figure 2b). With this method, the strain is evaluated $\approx -0.19\%$ in the pristine, in good agreement with the W-H analysis. A peak shift to higher $2\theta$ is observed at a higher fluence of $5 \times 10^{15}$ cm$^{-2}$, which is interpreted due to the introduction of a high number of defects, restoring compressive strain after irradiation to $\approx -0.16\%$. We have thus evidenced a method to relax the initial compressive strain for protons irradiation fluences of $10^{13}$ and $10^{14}$ cm$^{-2}$. To directly assess the impact of irradiation defects and the role of strain on the optoelectronic properties, we can correlate the PL spectra and lifetime with the structural changes presented here, as discussed in the following section.

## 3. Strain—Lifetime Correlation

It is known that lattice strain is directly associated with a high defect concentration that contributes to a higher non-radiative recombination rate, degrading the optoelectronic properties of the TC-MHP.[14] Figure 2e shows the lattice strain together with carrier lifetime as a function of irradiation fluence. We find that samples with lower emission intensity and carrier lifetime correspond to compressive strain. In contrast, the samples irradiated with a fluence of $10^{13}$ and $10^{14}$ cm$^{-2}$ show higher PL emission and longer carrier lifetime for a relaxed strain state, as shown in Figures 1 and 2e.

The carrier lifetime increases along with a change in relative strain from $-0.15\%$ to $-0.08\%$ at a moderate fluence of $10^{13}$ and $10^{14}$ ions cm$^{-2}$. For the pristine sample the average lifetime is ≈495 ns, which increases to ≈588 ns at $10^{13}$ ions cm$^{-2}$ and ≈1 µs at $10^{14}$ ions cm$^{-2}$. This behavior might be associated with irradiation-induced annealing of native points defects (introduced during film growth), associated with strain release as illustrated in Figure 2d. However, we checked the effect of conventional annealing at 350 K for 1 h, which did not result in any lifetime change. During synthesis, the samples are processed at 350 K for solvent evaporation and films crystallization. This kind of thin films can easily be damaged for higher annealing temperatures, so we decided to anneal for 1 h at that temperature. We observed steady lifetime values, indicating the process did not lower the defect density. Interestingly, the carrier lifetime is shown to decrease along with the introduction of compressive strain in the lattice from ≈−−0.08% to ≈−0.19% at higher irradiation fluences ($5 \times 10^{14}$ to $5 \times 10^{15}$ cm$^{-2}$). This effect is related to the formation of high-density point defects and disorder in the lattice, which leads to the introduction of a compressive strain. Generally, lattice strain induces lattice deformation and perturbs the electronic band structure of the material and thus consequently affects the carrier lifetime. At moderate fluence, the strain relaxation expands the lattice constant, increasing the carrier delocalization distance and slowing the carrier recombination process. Therefore, carrier lifetime increases during the strain relaxation process.[33] On the other hand, compressive strain arises at higher fluences ($10^{15}$ to $5 \times 10^{15}$ cm$^{-2}$) which reduce the lattice constant along with the introduction of a high-density of defects. This compressive strain decreases the carrier delocalization distance. It accelerates the carrier recombination process (shorter lifetime), as already observed with optical experiments under thin film bending to apply tensile or compressive strain.[33]

## 4. Impact of Irradiation Defects on Phase Segregation

The light-induced ion migration leading to phase segregation in mixed halide perovskites has been extensively studied these recent years.[34–37] In our previous study we addressed the photo-induced halide ion migration and quantitatively rationalized the spectroscopic processes during phase separation using time-resolved photoluminescence spectroscopy tools.[21] Our analysis revealed that laser excitation creates iodide- and bromide-rich domains associated with bandgap reduction of perovskite films as represented schematically in **Figure 3**c. With increasing laser power density, a continuous redshift in the emission peak from 762 nm at 0.1 mW cm$^{-2}$ up to 794 nm at 800 mW cm$^{-2}$ was observed at 300 K along with an increase in decay lifetime, which could be attributed to the halide ion migration induced phase segregation effect together with trap-filling. The bandgap reduction and growth of iodide and bromide-rich domains strongly depend on laser excitation power. PL measurements have allowed us to estimate the phase segregation rate (redshift) under laser illumination and the recovery rate under dark conditions, as the process is fully reversible. The process was observed to be fully reversible under dark conditions, and the relaxation process showed exponential dependency with time. It was found much faster at higher temperatures (330 K) than at room temperature. Using the recovery rate values at different temperatures, the activation energy for halide ion migration is calculated and found to be ≈0.31 eV.[21] In the present study, we have performed PL measurements at room temperature (296 K) on pristine and irradiated films at different fluences to provide insight into the photo-excitation-induced modification in segregation rate and change in activation energy for halide ion migration under different defects concentration and strain state. The measurements were performed at a laser power density of 55 mW cm$^{-2}$ to track the complete segregation process, as shown in Figure 3a and Figure S5, Supporting Information. We have evidenced a strong red-shift from ≈1.62 eV to ≈1.56 eV that we attribute to phase segregation and recombination in iodine-rich clusters as already observed.[21] The PL intensity also shows a strong increase with the redshift about 1 h before stabilization, indicating that the radiative recombination occurs in less defective regions as these are progressively enriched with the mobile iodine ions. The phase segregation mechanism is fully reversible, as shown in Figure 3b, where both peak position and PL intensity return to their initial values when the sample is kept under dark conditions for ≈7 h at room temperature. From the evolution of the PL peak position with time under light

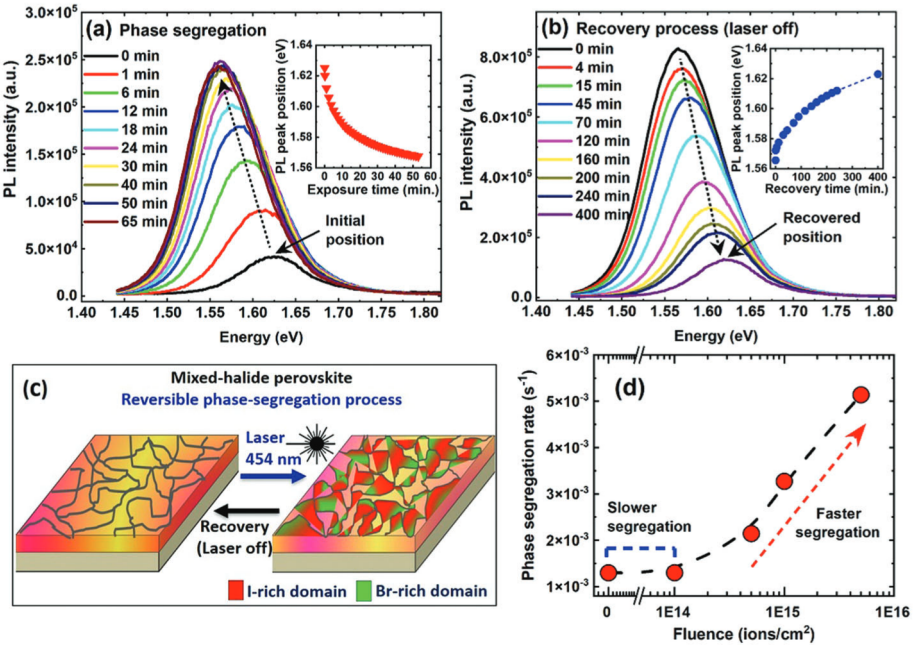


**Figure 3.** a) Time-dependent red-shift in PL emission and evolution of PL spectra under the influence of iodide-rich domains formation under continuous wave excitation ($P_{exc}$ = 55 mW cm$^{-2}$). Inset: PL peak position as a function of light exposure time. b) Time-dependent recovery process of phase segregated TC-MHP film under dark conditions (laser off). Inset: PL peak position as a function of time. c) Schematic picture of light-induced phase segregation and recovery. d) Phase segregation rate as a function of proton irradiation fluence. The dashed line is a guide to the eye.

exposure at a fixed power (≈55 mW cm$^{-2}$ here), one can obtain the segregation rate, which is about 1.3 × 10$^{-3}$ s$^{-1}$ for the pristine sample. As shown in Figure 3d, this value is not affected by irradiation at 10$^{14}$ cm$^{-2}$, which appears to be the threshold above which it significatively increases. The segregation rate shows to be proportional to the log of the fluence, increasing fourfold up to more than 5 × 10$^{-3}$ s$^{-1}$ at the fluence maximum of 5 × 10$^{15}$ cm$^{-2}$. Thus, it confirms that the phase segregation process is defect-mediated as the iodine diffusion under light should process through a pair exchange mechanism. It was discussed that the driving force for iodine diffusion might rely on trapped photogenerated holes that would have the ability to accumulate at different charge carrier traps.[35] It was also shown through optical measurements under hydrostatic pressure that lattice compression increases the activation barrier for phase segregation.[38] Studying the recovery process after phase segregation at variable temperature allows us to get the activation energies as illustrated in **Figure 4**. We found these activation energies are consistent with our previous study.[21] For the study presented here, we obtained consistent values with ≈0.29 eV for the recovery of the pristine sample. This value was obtained from the linear fit of the log of the recovery rate, as presented in Figure 4, using the PL data of recovery process at different temperatures (see Figure S6, Supporting Information). After ion irradiation at 5 × 10$^{15}$ cm$^{-2}$, and consistent with faster phase segregation, we have obtained a value for the activation energy for the recovery ≈0.21 eV. At moderate fluence, the increased segregation rate is consistent with a lower activation barrier that would be expected when the growth strain is released through ion irradiation, and consistent with the measurements under hydrostatic pressure.[38] However, at the highest fluence we have shown that a compressive strain is

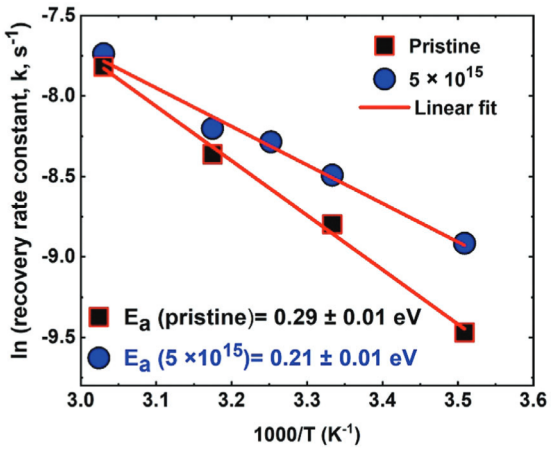


**Figure 4.** Arrhenius plots of ln (recovery rate constants) versus 1000/$T$ for determination of activation energies of halide ion migration during recovery processes of the pristine and irradiated film with a fluence of 5 × 10$^{15}$ cm$^{-2}$.

restored through defect accumulation. Both strain state and defect concentrations are thus important parameters to consider, the last one being predominant for ion diffusion at a high irradiation fluence.

## 5. Bound Excitons and Impurity Scattering Revealed with Low-Temperature PL

The low-temperature PL emission characteristics have also been investigated in pristine and irradiated samples at $T$ = 10 K,

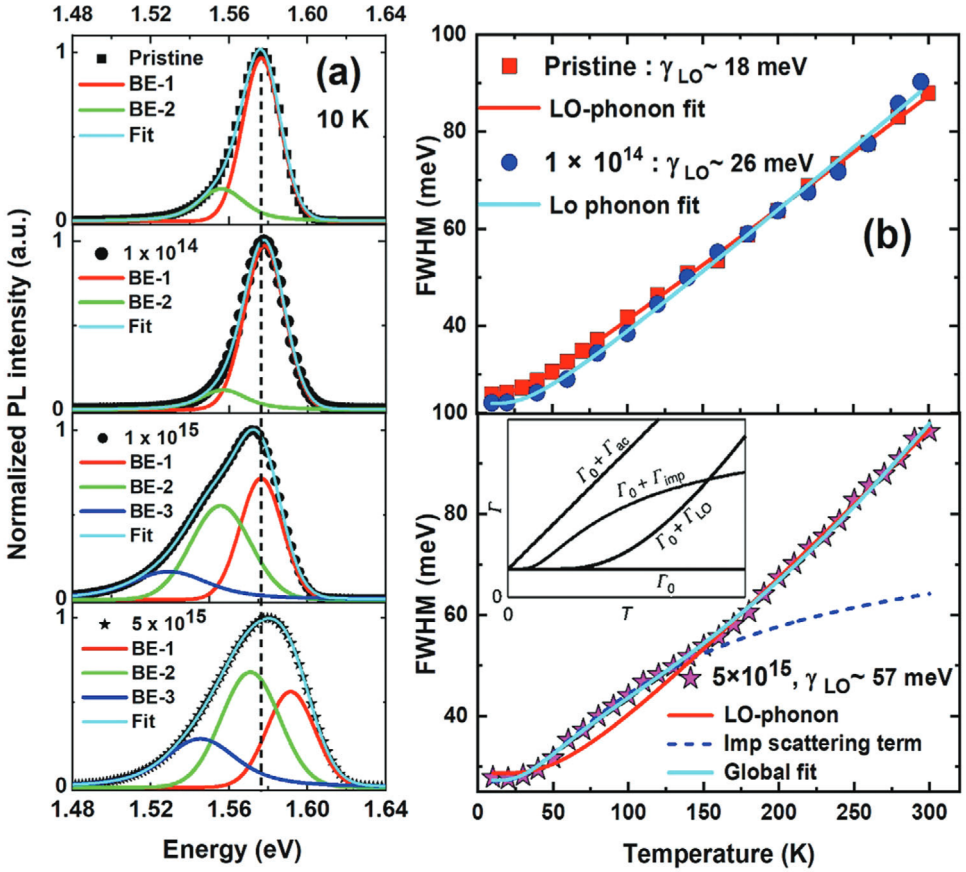


**Figure 5.** a) Photoluminescence spectra measured at $T = 10$ K of triple-cation mixed-halide perovskite film for pristine and different irradiation fluences. b) The linewidth broadening of PL spectra as a function of temperature (symbols) along with least square fitting curves (solid lines) to determine the exciton-phonon coupling for the pristine and irradiated film at $10^{14}$ cm$^{-2}$ (higher panel) and irradiated film at $5 \times 10^{15}$ cm$^{-2}$ (lower panel). Inset: Schematics to indicate the evolution of the different components to describe the peak broadening with temperature: $\Gamma_0$, $\Gamma_{ac}$, $\Gamma_{LO}$, $\Gamma_{imp}$, respectively the inhomogeneous broadening, the acoustic and longitudinal optical phonon scattering terms and the impurity scattering term.

as represented in **Figure 5**a. As previously shown in both single crystals and polycrystalline samples of $CH_3NH_3PbI_3$, the low-temperature emission spectra identify three bands that can be tentatively attributed to three different bound excitons recombinations.[22] The three processes are attributed to different energy levels lying near or inside the band gap. They are quoted $BE_1$, $BE_2$, and $BE_3$ as they get deeper inside the forbidden band. The pristine sample shows the presence of $BE_1$ and $BE_2$ recombinations, which can be first associated with near-band edge recombinations through iodine vacancies and interstitials, as these defects being the predominant ones after growth.[4,7,11,39] Irradiation at $10^{14}$ cm$^{-2}$ induces little change in the low-temperature PL spectrum. It rather evidences a decrease of the $BE_2$ relative contribution, consistent with strain relieving. At higher fluence ($10^{15}$ cm$^{-2}$), the $BE_1$ energy does not change, but one can observe that the $BE_2$ relative contribution strongly increases, while the $BE_3$ contribution grows ≈20 meV below the $BE_2$. This growing $BE_3$ contribution could be associated with the growing number of lead vacancies and interstitials after irradiation. Several calculations show that the methylammonium molecule does not generate in-gap states.[4,40] At a high fluence of $5 \times 10^{15}$ cm$^{-2}$, the gap is modified and the $BE_1$ contribution is shifted ≈20 meV higher, together with $BE_2$ and $BE_3$ processes. The $BE_1$ contribution is relatively lowered as the recombination through the inner band-gap defect states may be associated with iodine and lead point defects, which evidences a growing contribution at high concentrations (higher irradiation fluence). We have also studied the temperature dependence of the PL spectra from 10 K to room temperature at 300 K as presented in the Section S7, Supporting Information. The decomposition in several components allows focusing only on the $BE_1$ contribution changes when the temperature increases. We can follow the band broadening with temperature increase from the analysis, as represented in Figure 5b. We can describe the broadening using Segall's expression[21,41]

$$\Gamma = \Gamma_{inh} + \Gamma_{ac} + \Gamma_{LO} + \Gamma_{imp} \tag{3}$$

$$\Gamma = \Gamma_{inh} + \gamma_{ac} T + \frac{\gamma_{LO}}{\exp\left(\frac{\hbar\omega_{LO}}{k_B T}\right) - 1} + \gamma_{imp} \exp\left(-\frac{E_b}{k_B T}\right) \tag{4}$$

In the Equations (3) and (4), the broadening is expressed as a sum of different contributions, where $\Gamma_{inh}$ is the inhomogeneous broadening contribution that arises from scattering due

to exciton-exciton interaction and crystal disorder, and is temperature independent. Also, $\Gamma_{ac} = \gamma_{ac} T$ and $\Gamma_{LO}$ are the different homogeneous broadening terms resulting from acoustic and longitudinal optical (LO)-phonon (Fröhlich coupling) scattering. The terms $\gamma_{ac}$ and $\gamma_{LO}$ in Equation (2) represent the charge carrier–phonon coupling strengths with, respectively, acoustic and optical phonons. The last term $\Gamma_{imp}$ accounts for the scattering due to ionized impurities with average binding energy $E_b$. We have neglected the impurity broadening term for the pristine and low irradiation fluence. We can observe from Figure 5b that the fits using the expression for the broadening as a function of temperature are very good and indicates an increasing coupling parameter $\gamma_{LO}$ from ≈18 meV with the pristine sample to ≈26 meV after irradiation at $10^{14}$ cm$^{-2}$. At the same time, the phonon energy is kept almost constant at ≈8 meV. As a matter of comparison, the same method was used for several hybrid perovskite materials, giving $\gamma_{LO}$ ≈11.5 meV and $E_{LO}$ ≈ 40 meV for $CH_3NH_3PbI_3$.[42] In our TC-MHP sample, the electron–phonon coupling is higher than this value. At the same time, the phonon energy we obtained is much lower but closer to the expected value from vibrational studies, which is $E_{LO}$ ≈ 11 meV for $CH_3NH_3PbI_3$.[2] The increase in LO-phonon coupling parameter with ion irradiation may be due to the defect number increase and to the strong interaction of phonons with trapped charge carriers. At a higher fluence of $5 \times 10^{15}$ cm$^{-2}$, while the LO-phonon energy stays almost constant ≈10 meV, the electron–phonon coupling still increases to $\gamma_{LO}$ ≈ 57 meV indicating a high coupling for a high defect concentration. It is also striking to note that for high irradiation fluence and high defect concentration, one must consider the impurity scattering term $\Gamma_{imp}$ in the model to describe the PL line broadening with temperature properly. At a higher fluence of $5 \times 10^{15}$ cm$^{-2}$, the experimental data are fitted well by considering the contributions of ionized impurities scattering term with LO-phonon scattering term. From the model, we obtain an activation energy ≈22 meV for the impurity scattering term. Interestingly, as shown in the Figure S8, Supporting Information, we can analyze the temperature dependence of the PL integrated intensity with an Arrhenius activation law. The thermal quenching of the PL intensity can be described by the familiar expression[43]

$$I(T) = \frac{I_0}{1 + C \cdot \exp\left(-\frac{E_a}{k_B T}\right)} \quad (5)$$

where, $I_0$ is the PL intensity at $T = 0$ K, $E_a$ is the activation energy for the non-radiative processes, $C$ is a constant and $k_B$ is Boltzmann constant. This analysis shows that the activation energy for non-radiative recombinations is ≈31 meV in the pristine sample, in good agreement with the exciton binding energy estimated ≈24–32 meV in $(CH_3NH_3)PbI_3$ and a little bit lower for Cs-containing mixed perovskite compounds ≈20–24 meV.[44] However, irradiation at $10^{14}$ protons cm$^{-2}$ indicate an increase of that value to ≈45 meV that could be attributed to the strain relief we have evidenced. At higher fluence, when the compressive strain is restored and in the presence of a high defect concentration, the activation energy for non-radiative recombination decreases to ≈19 meV. It is very interesting to observe a change in the activation energy with strain state that could be interpreted as a change in exciton binding energy, giving a possible explanation for the value dispersion obtained from different studies.[45]

## 6. Conclusion

Defect tolerance has become a challenge to improve efficiencies in the frame of photovoltaic devices and have been a vital issue in understanding hybrid perovskite materials. We have introduced different defect concentrations with 1 MeV proton irradiation into mixed halide perovskites polycrystalline thin films. Contrary to usual semiconductors, where irradiation defects quench the luminescence very efficiently, we observe high radiation hardness. Electronic energy deposition, which is the primary mechanism during the proton irradiation, is shown to relax growth strain, resulting in considerable exciton lifetime improvement from about 500 ns to ≈1 µs for a fluence of $10^{14}$ cm$^{-2}$. Higher irradiation fluence at $5 \times 10^{15}$ cm$^{-2}$ is shown to restore compressive strain and leads to sample degradation, with lower lifetime value ≈200 ns. We confirmed that the phase segregation occurring under light illumination in mixed halide perovskites is clearly shown to be defects mediated as the segregation rate increases by four at the highest proton irradiation fluence. Also, the near band-edge energy levels of irradiation defects and the associated bound exciton mechanisms are revealed with low-temperature photoluminescence. Additionally, temperature dependent PL gives some insight into the electron–phonon coupling mechanism and their modification with ion irradiation, as we evidenced an increase in electron–phonon coupling parameter from ≈18 to ≈57 meV for a fluence of $10^{15}$ cm$^{-2}$. We have shown that proton irradiation in hybrid perovskite materials is an effective way to tune both strain and defect concentration, opening a new perspective in sample post-processing using high-energy and low irradiation fluences.

## 7. Experimental Section

*Sample Preparation*: The triple-cation mixed halide hybrid perovskite thin films (thickness 380 nm) were prepared using the spin coating technique on glass substrates. At first, for the materials synthesis, the $(MA_{0.17}FA_{0.83})Pb(I_{0.83}Br_{0.17})_3$ perovskite precursor solution was prepared by dissolving $PbI_2$ (1.1 M), FAI (1.0 M), $PbBr_2$ (0.2 M), MABr (0.2 M) in a 75 wt% mixture of anhydrous *N*,*N*-dimethylformamide (DMF) and dimethyl sulfoxide (DMSO). The solution was kept on stirring, and then 42 µL (5% molar ratio) of CsI (1.5 M in DMSO) was added to the resultant solution at room temperature. The precursors of FAI and $PbI_2$ were purchased from Sigma Aldrich; MABr from Solaronix; $PbI_2$, and CsI from Alfa Aesar. Before thin film coating, glass substrates were initially cleaned in deionized water, acetone, and 2-propanol sequentially by ultra-sonication, followed by drying in dry nitrogen gas. A dynamic dispense was generally preferred in the synthesis process as it is a more controlled process that produces less substrate-to-substrate variation. The triple-cation solution was dispensed after stabilizing the spin revolution at 6000 rpm. The total spinning time was 30 s, and then 200 µL of chlorobenzene was dropped for 5 s to remove residual solvent. Films were annealed at 80 °C in nitrogen ambient for 1 h, allowing solvent evaporation and thin film crystallization.

*Experimental Details*: The proton ion irradiation was performed using the van de Graaf ARAMIS accelerator at the IJC laboratory at Paris-Saclay University. An ion energy of 1 MeV and fluences between $10^{13}$ and $5 \times 10^{15}$ cm$^{-2}$ were used. The ion beam size was 1 mm and was rastered over a large area to have a homogeneous dose deposition. The implantations were performed at room temperature with ion currents about 1 µA in order to keep maximum deposited power below 100 mW cm$^{-2}$.

The UV–vis absorption measurements were performed using Cary 5000 UV–vis–NIR double-beam spectrophotometer. Photoluminescence spectroscopy studies on mixed halide perovskite samples were performed in reflection geometry with a Quantamaster spectrometer from Horiba-JY equipped with an R13456 photomultiplier (Hamamatsu) detector. A fiber-coupled laser diode (MDL-III-454nm) from CNI was used; it had a wavelength of 454 ± 5 nm at different excitation powers and was focused on the sample on a spot size of ≈1.75 mm diameter. The time-resolved single photon counting (TCSPC) measurements were carried out using as an excitation source a Picoquant laser at 448 nm (LDH-IB-440-B) controlled by Taïko PDL M1 with adjustable frequency up to 100 MHz and pulse width below 80 ps. For low-temperature measurements, the samples were glued with silver paste in an optical closed-cycle cryostat from ARS Instruments equipped with two quartz windows, allowing control of the sample temperature from 10 to 400 K. The X-ray diffraction measurements were performed using a four-circle diffractometer with Cu rotating anode (wavelength $\lambda_{K_\alpha}$ = 1.54 Å). X-ray diffraction measurements were performed with Cu $K\alpha$ radiation generated by a Rigaku RU-300B rotating anode. The sample was mounted on a 4-circle Eulerian Huber diffractometer, and the diffraction signal was recorded in specular geometry with a Timepix detector from Amsterdam Scientific Instruments. The diffractograms were obtained by integration of the diffraction rings on the 2D detector with an angular resolution of 0.01° in $2\theta$.

## Supporting Information

Supporting Information is available from the Wiley Online Library or from the author.

## Acknowledgements

This work was supported by the LabEx PALM (ANR-10-LABX-0039-PALM) as part of France 2030 programme ANR-11-IDEX-0003. The authors acknowledge Cyril Bachelet and Jérôme Bourçois for the proton irradiations using the ARAMIS accelerator at IJClab in Orsay.

## Conflict of Interest

The authors declare no conflict of interest.

## Data Availability Statement

The data that support the findings of this study are available from the corresponding author upon reasonable request.

## Keywords

ion irradiation, mixed-halide perovskites, optoelectronic properties, phase segregation, strain engineering

Received: March 10, 2023
Published online:

[1] F. Li, C. Ma, H. Wang, W. Hu, W. Yu, A. D. Sheikh, T. Wu, *Nature Commun.* **2015**, *6*, 8238.
[2] L. M. Herz, *ACS Energy Lett.* **2017**, *2*, 1539.
[3] R. L. Milot, G. E. Eperon, H. J. Snaith, M. B. Johnston, L. M. Herz, *Adv. Funct. Mater.* **2015**, *25*, 6218.
[4] A. Maiti, S. Chatterjee, L. Peedikakkandy, A. J. Pal, *Sol. RRL* **2020**, *4*, 2000505.
[5] a) W.-J. Yin, T. Shi, Y. Yan, *Appl. Phys. Lett.* **2014**, *104*, 063903; b) W.-J. Yin, J.-H. Yang, J. Kang, Y. Yan, S.-H. Wei, *J. Mater. Chem. A* **2015**, *3*, 8926.
[6] Q. Wang, Y. Shao, H. Xie, L. Lyu, X. Liu, Y. Gao, J. Huang, *Appl. Phys. Lett.* **2014**, *105*, 163508.
[7] A. Musiienko, D. R. Ceratti, J. Pipek, M. Brynza, H. Elhadidy, E. Belas, M. Betusiak, G. Delport, P. Praus, *Adv. Funct. Mater.* **2021**, *31*, 2104467.
[8] A. Walsh, A. Zunger, *Nat. Mater.* **2017**, *16*, 964.
[9] D. A. Egger, A. Bera, D. Cahen, G. Hodes, T. Kirchartz, L. Kronik, R. Lovrincic, A. M. Rappe, D. R. Reichman, O. Yaffe, *Adv. Mat.* **2018**, *30*, 1800691.
[10] J. M. Ball, A. Petrozza, *Nat. Energy* **2016**, *1*, 16149.
[11] G.-W. Kim, A. Petrozza, *Adv. Energy Mater.* **2020**, *10*, 2001959.
[12] D. Liu, D. Luo, A. N. Iqbal, K. W. P. Orr, T. A. S. Doherty, Z.-H. Lu, S. D. Stranks, W. Zhang, *Nat. Mater.* **2021**, *20*, 1337.
[13] C. Zhu, X. Niu, Y. Fu, N. Li, C. Hu, Y. Chen, X. He, G. Na, P. Liu, H. Zai, Y. Ge, Y. Lu, X. Ke, Y. Bai, S. Yang, P. Chen, Y. Li, M. Sui, L. Zhang, H. Zhou, Q. Chen, *Nat. Commun.* **2019**, *10*, 815.
[14] T. W. Jones, A. Osherov, M. Alsari, M. Sponseller, B. C. Duck, Y.-K. Jung, C. Settens, F. Niroui, R. Brenes, C. V. Stan, Y. Li, M. Abdi-Jalebi, N. Tamura, J. E. Macdonald, M. Burghammer, R. H. Friend, V. Bulović, A. Walsh, G. J. Wilson, S. Lilliu, S. D. Stranks, *Energy Environ. Sci.* **2019**, *12*, 596.
[15] M. Saliba, T. Matsui, J. Y. Seo, K. Domanski, J. P. Correa-Baena, M. K. Nazeeruddin, S. M. Zakeeruddin, W. Tress, A. Abate, A. Hagfeldt, M. Grätzel, *Energy Environ. Sci.* **2016**, *9*, 1989.
[16] W. Rehman, D. P. McMeekin, J. B. Patel, R. L. Milot, M. B. Johnston, H. J. Snaith, L. M. Herz, *Energy Environ. Sci.* **2017**, *10*, 361.
[17] K. A. Bush, K. Frohna, R. Prasanna, R. E. Beal, T. Leijtens, S. A. Swifter, M. D. McGehee, *ACS Energy Lett.* **2018**, *3*, 428.
[18] M. Malekshahi, C. Otero-Martìnez, J. Ye, W. Zuo, L. Manna, M. Saliba, R. L. Z. Hoye, L. Polavarapu, *Adv. Optical Mater.* **2022**, *10*, 2200423.
[19] E. T. Hoke, D. J. Slotcavage, E. R. Dohner, A. R. Bowring, H. I. Karunadasa, M. D. McGehee, *Chem. Sci.* **2015**, *6*, 613.
[20] H. Zhang, X. Fu, Y. Tang, H. Wang, C. Zhang, W. W. Yu, X. Wang, Y. Zhang, M. Xiao, *Nat. Commun.* **2019**, *10*, 1088.
[21] S. K. Gautam, M. Kim, D. R. Miquita, J.-E. Bourée, B. Geffroy, O. Plantevin, *Adv. Funct. Mater.* **2020**, *30*, 2002622.
[22] O. Plantevin, S. Valère, D. Guerfa, F. Lédée, G. Trippé-Allard, D. Garrot, E. Deleporte, *Phys. Status Solidi B* **2019**, *256*, 1900199.
[23] S. Kanaya, G. M. Kim, M. Ikegami, T. Miyasaka, K. Suzuki, Y. Miyazawa, H. Toyota, K. Osonoe, T. Yamamoto, K. Hirose, *J. Phys. Chem. Lett.* **2019**, *10*, 6990.
[24] W. O. Herrera Martínez, N. B. Correa Guerrero, V. A. Gómez Andrade, M. Alurralde, M. Dolorez Perez, *Sol. Energy Mater. Sol. Cells* **2022**, *238*, 111644.
[25] F. Lang, N. H. Nickel, J. Bundesmann, S. Seidel, A. Denker, S. Albrecht, V. V. Brus, J. Rappich, B. Rech, G. Landi, H. C. Neitzert, *Adv. Mater.* **2016**, *28*, 8726.
[26] V. V. Brus, F. Lang, J. Bundesmann, S. Seidel, A. Denker, B. Rech, G. Landi, H. C. Neitzert, J. Rappich, N. H. Nickel, *Adv. Electron. Mater.* **2017**, *3*, 1600438.
[27] F. Lang, M. Jost, J. Bundesmann, A. Denker, S. Albrecht, G. Landi, H.-C. Neitzert, J. Rappich, N. H. Nickel, *Energy Environ. Sci.* **2019**, *12*, 1634.
[28] F. Lang, M. Jost, K. Frohna, E. Köhnen, A. Al-Ashouri, A. R. Bowman, T. Bertram, A. B. Morales-Vilches, D. Koushik, E. M. Tennyson, K. Galkowski, G. Landi, M. Creatore, B. Stannowski, C. A. Kaufmann, J. Bundesmann, J. Rappich, B. Rech, A. Denker, S. Albrecht, N. Heinz-Christoph, N. H. Nickel, S. D. Stranks, *Joule* **2020**, *4*, 1054.
[29] J. Ziegler, J. Biersack, U. Littmark, *The Stopping of Ions in Matter*, Pergamon, New York **1985**.

[30] M. J. Trimpl, A. D. Wright, K. Schutt, L. R. V. Buizza, Z. Wang, M. B. Johnston, H. J. Snaith, P. Mller-Buschbaum, L. M. Herz, *Adv. Funct. Mat.* **2020**, *30*, 2004312.
[31] S. D. Stranks, V. M. Burlakov, T. Leijtens, J. M. Ball, A. Goriely, H. J. Snaith, *Phys. Rev. Appl. 2*, 034007.
[32] H. Tsai, R. Asadpour, J. C. Blancon, C. C. Stoumpos, O. Durand, J. W. Strzalka, B. Chen, R. Verduzco, P. M. Ajayan, S. Tretiak, J. Even, M. Ashraf Alam, M. G. Kanatzidis, W. Nie, A. D. Mohite, *Science* **2018**, *360*, 67.
[33] C. Wang, L. Ma, D. Guo, X. Zhao, Z. Zhou, D. Lin, F. Zhang, W. Zhao, J. Zhang, Z. Nie, *J. Mater. Chem. C* **2020**, *8*, 3374.
[34] S. G. Motti, J. B. Patel, R. D. J. Oliver, H. J. Snaith, M. B. Johnston, L. M. Herz, *Nat. Commun.* **2021**, *12*, 6955.
[35] J. T. DuBose, P. V. Kamat, *Acc. Mater. Res.* **2022**, *3*, 761.
[36] K. Frohna, M. Anaya, S. Macpherson, J. Sung, T. A. S. Doherty, Y.-H. Chiang, A. J. Winchester, K. W. P. Orr, J. E. Parker, P. D. Quinn, K. M. Dani, A. Rao, S. D. Stranks, *Nat. Nanotechnol.* **2022**, *17*, 190.
[37] V. J.-Y. Lim, A. J. Knight, R. D. J. Oliver, H. J. Snaith, M. B. Johnston, L. M. Herz, *Adv. Funct. Mater.* **2022**, *32*, 2204825.
[38] L. A. Muscarella, E. M. Hutter, F. Wittmann, Y. Won Woo, Y.-K. Jung, L. McGovern, J. Versluis, A. Walsh, H. J. Bakker, B. Ehrler, *ACS Energy Lett.* **2020**, *5*, 3152.
[39] Y. Rakita, I. Lubomirsky, D. Cahen, *Mater. Horiz.* **2019**, *6*, 1297.
[40] W.-J. Yin, J. H. Yang, J. Kang, Y. Yan, S.-H. Wei, *J. Mater. Chem. A* **2015**, *3*, 8926.
[41] S. Rudin, T. L. Reinecke, B. Segall, *Phys. Rev. B* **1990**, *42*, 11218.
[42] A. Wright, C. Verdi, R. L. Milot, G. E. Eperon, M. A. Pérez-Osorio, H. J. Snaith, F. Giustino, M. B. Johnston, L. M. Herz, *Nat. Commun.* **2016**, *7*, 11755.
[43] D. Bimberg, M. Sondergeld, E. Grobe, *Phys. Rev. B* **1971**, *4*, 3451.
[44] F. Ruf, M. F. Aygüler, N. Giesbrecht, B. Rendenbach, A. Magin, P. Docampo, H. Kalt, M. Hetterich, *APL Mater.* **2019**, *7*, 031113.
[45] D. M. Niedzwiedzki, H. Zhou, P. Biswas, *J. Phys. Chem. C* **2022**, *126*, 1046.